Modifying the polarization state of terahertz radiation using anisotropic twin-domains in $LaAlO_3$

J. Lloyd-Hughes,[1,*] S. P. P. Jones,[2] E. Castro-Camus,[3] K. I. Doig,[2] and J. L. MacManus-Driscoll[4]

[1]University of Warwick, Department of Physics, Gibbet Hill Road, Coventry CV4 7AL, UK

[2]University of Oxford, Department of Physics, Clarendon Laboratory, Parks Road, Oxford OX1 3PU, UK

[3]Centro de Investigaciones en Óptica A C, Loma del Bosque 115, Lomas del Campestre, Leon, Guanajuato 37150, Mexico

[4]Department of Materials Science, University of Cambridge, 27 Charles Babbage Road, Cambridge CB3 0FS, UK

*Corresponding author: j.lloyd-hughes@warwick.ac.uk

Received December 27, 2013; accepted January 10, 2014;
posted January 15, 2014 (Doc. ID 203477); published February 18, 2014

Polarization-resolved terahertz (THz) time-domain spectroscopy was utilized to examine the complex refractive index of lanthanum aluminate ($LaAlO_3$), a rhombohedrally distorted perovskite that exhibits crystallographic twin domains. The uniaxial anisotropy of the refractive index was quantified. The ellipticity of THz radiation pulses after transmission through single domains indicated that $LaAlO_3$ can be used as a quarter- or half-wave plate. The effective anisotropy of [001]-oriented $LaAlO_3$ was found to be reduced when the material exhibited multiple, narrow twin domains.

OCIS codes: (260.1440) Birefringence; (260.2130) Ellipsometry and polarimetry; (320.7150) Ultrafast spectroscopy; (260.2710) Inhomogeneous optical media.

http://dx.doi.org/10.1364/OL.39.001121

Oxides with perovskite-like structures exhibit a wealth of functional properties, such as magnetoelectric multiferroicity [1], two-dimensional conductivity [2], and interfacial superconductivity [3]. In its bulk room-temperature phase, lanthanum aluminate ($LaAlO_3$) is a rhombohedrally distorted perovskite that undergoes an improper ferroelastic transition at 820 K to a cubic phase [4]. $LaAlO_3$ features prominently in different oxide heterostructures: it is often used as a substrate for epitaxial films of high-temperature cuprate superconductors and multiferroics such as $BiFeO_3$ [5]. Furthermore, epitaxial $LaAlO_3/SrTiO_3$ interfaces support two-dimensional conduction with high mobility [2] above a critical $LaAlO_3$ thickness of three unit cells, and which can be patterned with conductive nanowires by atomic force microscopy [6].

The electronic, elastic, structural, and optical properties of bulk $LaAlO_3$ have been investigated previously using a variety of methods that include neutron diffraction [4], ultrasonics [7], and first-principles calculations [8,9]. Raman scattering and Fourier-transform spectroscopy have unveiled the influence of the rhombohedral distortion on the vibrational modes of $LaAlO_3$ [4,10,11]. Terahertz (THz) time-domain spectroscopy (TDS) was used previously to examine the complex refractive index $\tilde{n} = n + i\kappa$ in [001]-oriented $LaAlO_3$ [12,13] below the lowest frequency optical phonons. Grischkowsky and Keiding reported a refractive index n that increased monotonically from 4.9 at 0.1 THz to 5.1 at 2.0 THz, characteristic of dispersion below an optical phonon frequency, and detected no noticable birefringence [12]. Zou *et al.* reported that thermal annealing at 1273 K modified the complex THz refractive index in the range below 3 THz by creating features similar to three resonant absorption lines [13], and did not discuss any birefringence. However, uniaxial anisotropy of the refractive index (and therefore birefringence) is expected for $LaAlO_3$ at room temperature, owing to its rhombohedral unit cell [14].

In this Letter a study of optical anisotropy in $LaAlO_3$ at THz frequencies is reported. Polarization-resolved THz-TDS [15] was used to determine the complex refractive index for different crystallographic orientations. Control of the THz polarization state is demonstrated, rotating linear polarization or producing circularly polarized THz radiation. The critical influence of twin domains in $LaAlO_3$ upon the anisotropic THz optical properties is highlighted.

THz-TDS [16] was utilized to determine $\tilde{n} = n + i\kappa$ of $LaAlO_3$ in the frequency range from 0.2 to 3.0 THz. Linearly polarized THz transients were normally incident onto the samples, and orthogonal components E_x and E_y of the transmitted THz pulses were measured using a $\langle 111 \rangle$-oriented ZnTe crystal [17]. Single crystals of $LaAlO_3$ were obtained from MTI Corporation (USA) with surface normals orientated along [001], [110], and [111] and thickness 0.5 mm. Optical polarization microscopy (Metripol, Oxford Cryosystems) in conjunction with high-resolution x-ray diffraction measurements of rocking curves determined that [001] samples were twinned, while [110] and [111] orientations exhibited no twins. Multiple [001] samples (denoted $[001]_A$ and $[001]_B$) exhibited different twin domain sizes, discussed in detail later in this Letter.

Below 820 K $LaAlO_3$ is a rhombohedrally distorted perovskite, with space group $R\bar{3}c$ [4]. This distortion along the threefold [111] axis, illustrated in Fig. 1(a), is small and a pseudocubic unit cell is often used. Herein, crystal orientations are denoted with respect to the cubic cell. Rhombohedral crystals are uniaxially birefringent [14], with a refractive index ellipsoid pictured in Fig. 1(b), in which the optical axis corresponds to the [111] direction. Cross-sections of this ellipsoid in a plane perpendicular to the light's propagation vector denote the polarization dependence of the refractive index, and are provided in Figs. 1(d), 1(f) and 1(h) for the three crystal orientations under investigation.

The refractive index n_{ij} is reported in Fig. 1(c) for the [111]-oriented $LaAlO_3$ crystal. Here, the subscripts i and j

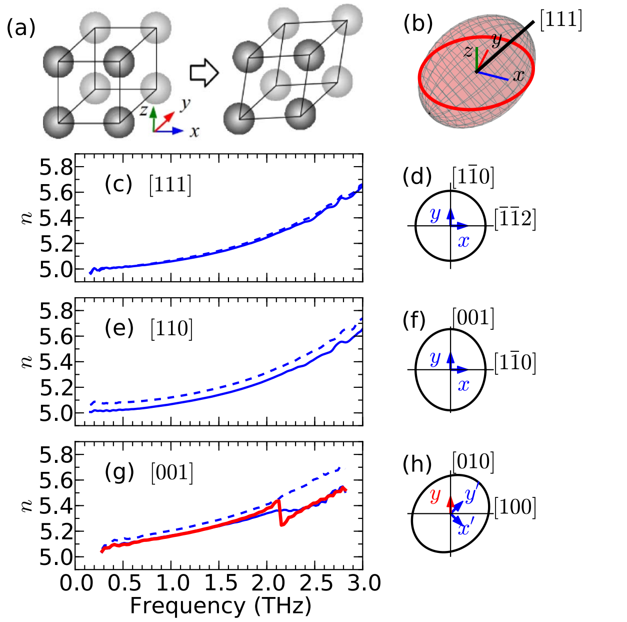

Fig. 1. (a) Rhombohedral distortion along [111] makes $LaAlO_3$ uniaxially birefringent. (b) Refractive index ellipsoid with optical axis along [111] (black line). The red line shows the $z = 0$ cross section, repeated in subplot (h). The THz refractive indices for different crystal orientations ([111], [110], and [001]) are shown in (c), (e), and (g), while (d), (f), and (h) show corresponding cross sections through the refractive index ellipsoid and measurement axis orientations. In (c), (e) the solid blue lines show n_{xx}, and the dashed lines show n_{yy}. In (g) the solid and dashed blue lines show $n_{x'x'}$ and $n_{y'y'}$, while the thick red line gives n_{yy}.

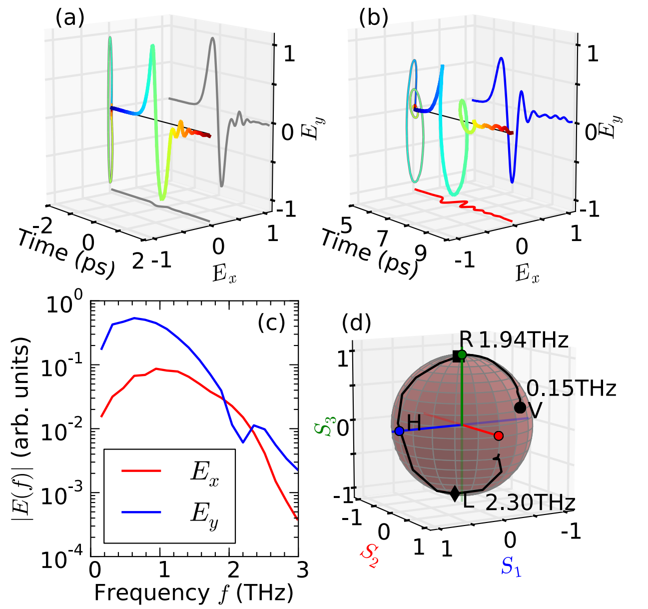

Fig. 2. Polarization-resolved THz electric field pulses for (a) the reference and (b) the $LaAlO_3$ sample $[001]_A$ (500 μm thick). (c) Amplitude spectra of data in (c). (d) Polarization state of THz radiation transmitted through sample A drawn on a unit Poincaré sphere.

denote the directions of the incident and transmitted THz electric field in the experimental coordinate system. The refractive index n_{xx} for x parallel to [$\bar{1}\,\bar{1}\,2$] (solid line) is identical to the refractive index n_{yy} along [1$\bar{1}$0] (dashed line). This is because the refractive index is independent of the polarization of the wave [Fig. 1(d)] for a ray propagating parallel to [111].

In contrast, for [110]-oriented $LaAlO_3$ the measured refractive index is a function of crystal orientation. Figure 1(e) illustrates that n_{xx} (solid line) is smaller than n_{yy} (dashed line), with a frequency-independent birefringence $\Delta n = n_{yy} - n_{xx} \simeq 0.06$. Here, x and y are as defined in Fig. 1(f). Similarly, [001]-oriented crystals exhibit a refractive index that depends upon the orientation of the THz electric field with respect to the crystal, as Fig. 1(g) demonstrates. Here, the measurements $n_{x'x'}$ (solid, thin line) and $n_{y'y'}$ (dashed, thin line) were obtained with the THz electric field along [1$\bar{1}$0] and [110] in order to probe the major and minor axes of the refractive index ellipse, shown in Fig. 1(h). In this case the birefringence increases with frequency, from $\Delta n(1.0\ \mathrm{THz}) = 0.038$ to $\Delta n(2.0\ \mathrm{THz}) = 0.070$.

In Fig. 1 the refractive index increases monotonically with frequency as a result of the lowest IR-active phonon modes, the A^1_{2u} singlet at 5.0 THz and the E^1_u doublet at 5.5 THz [8,10,11,18]. These modes derive from the threefold degenerate F_{1u} vibrations of the cubic Pm$\bar{3}$m phase [8]. In the rhombohedral phase octahedra rotate around [111] and are distorted from their ideal shape in the cubic phase, lifting this degeneracy. The modes arise from the displacement of Al-O octahedra with respect to the heavier La sublattice [8,11]. Transverse electromagnetic radiation propagating along [111] cannot couple to the A^1_{2u} mode [11], where the dipole moment is also along [111]. Therefore, the refractive index reported in Fig. 1(c) is that resulting from the E^1_u modes at 5.5 THz. At a given frequency in the experimental range n is higher when the A^1_{2u} mode contributes, as, e.g., for n_{yy} in Fig. 1(e), owing to the lower frequency of the A^1_{2u} mode. The splitting between A^1_{2u} and E^1_u modes, created by the rhombohedral distortion, is therefore the driving force for optical anisotropy in $LaAlO_3$ in the THz range.

When the THz electric field is polarized at intermediate angles between the fast and slow axes the $LaAlO_3$ will act like a waveplate, providing a phase delay for one component with respect to the other. Polarization-resolved THz waveforms are depicted in Fig. 2(a) for the reference pulse (in vacuum) and Fig. 2(b) after transmission through the $[001]_A$ sample with the THz electric field along [010]. While the incident pulse is linearly polarized in the y direction ($E_y \gg E_x$), the time-domain waveform is elliptical after the $LaAlO_3$ sample, with a substantial E_x component.

In Fig. 2(c) the amplitude spectra calculated from Fig. 2(b) are reported for E_x (red line) and E_y (blue line). Close to 2.1 THz there is a pronounced reduction in E_y, commensurate with a region, where E_x exceeds E_y. Without performing polarization-resolved THz detection this would appear to be an absorption line, creating a characteristic step in the refractive index n_{yy} [thick red line in Fig. 1(g)] and an absorption coefficient similar to that reported in Ref. [13]. However, rather than representing real physical absorption the anisotropy of the refractive index has resulted in a polarization rotation. This highlights the complexity of analyzing anisotropic media with THz-TDS, which standardly measures only one polarization channel (e.g. determining just $\tilde{n}_{xx}$). Other systems exhibiting anisotropy in the THz range have been reviewed recently [19–21].

To probe further the elliptical THz polarization after sample $[001]_A$, Fig. 2(d) shows a Poincaré sphere representation of the polarization state. Here, S_1, S_2, and S_3 are the normalized Stokes parameters, and the THz radiation varies from vertically polarized (V) at low frequency, through right-hand circular (R) at 1.94 THz to horizontal (H) and left-hand circular (L) at 2.30 THz.

The signed ellipticity $\epsilon(\omega) = \tan(\chi(\omega))$, where $\chi(\omega)$ is the angle of the major axis of the polarization ellipse to the x axis, can be used to quantify the development of the polarization with frequency [22]. In Fig. 3(a) the ellipticity is shown (solid line) for sample $[001]_A$ with the THz electric field along [010], corresponding to the data in Figs. 2(c) and 2(d). Here, $\epsilon = 0$ corresponds to linear polarization, as observed at low and high frequencies and at 2.1 THz. Right-handed ($\epsilon = +1$) and left-handed ($\epsilon = -1$) circular polarization states can also be witnessed. To confirm that this polarization modification arises from optical anisotropy this sample was reduced in thickness from 500 to 387 μm by mechanical polishing. The resulting ellipticity of the transmitted THz beam (dashed line) is shifted upward in frequency by 30%, commensurate with the reduction in thickness.

The modification of the polarization state of THz radiation by [001]-oriented $LaAlO_3$ depends sensitively upon the presence of twin domains in the crystal, as discussed in the following. Polarization microscopy of the pristine (as-received) sample $[001]_A$ at 550 nm revealed large twins, with domain walls running along [010] and domains up to 600 μm in width [Fig. 3(b)]. The color scale denotes the optical orientation, the angle of the slow axis from the horizontal. The domains are comparable in width to the diffraction-limited spot size of the THz beam, which samples only one or two domains. Sample $[010]_B$ exhibited smaller twin domains [Fig. 3(d)] of about 30 μm width. In this case the THz beam probes multiple (>10) domains with orientations differing by 90°. No substantial polarization rotation occurs in the range below 2 THz, as evidenced by the ellipticity ϵ reported in Fig. 3(c), which is similar with (solid line) and without (dashed line) the sample. Averaging propagation along the fast and slow axes of multiple domains produces an effective medium with reduced anisotropy (lower effective anisotropy).

For a medium with birefringence Δn and thickness d, the phase delay θ between the fast and slow axes at angular frequency ω is given by $\theta = \Delta n \omega d/c$. For a half-wave plate ($\theta = \pi$) at 2.1 THz with thickness 0.5 mm (as for sample $[001]_A$), therefore, we would predict $\Delta n_\pi = 0.143$. Here, the subscript denotes that the birefringence was obtained from the frequency at which $\theta = \pi$. However the birefringence calculated from the refractive index data in Fig. 1(g) was lower, at $\Delta n = n_{y'y'} - n_{x'x'} = 0.070$, perhaps as a consequence of probing more than one domain. The reduced effective anisotropy of sample $[001]_B$ requires a larger frequency to create $\theta = \pi$: as witnessed in Fig. 3(c), this condition is not satisfied below 3.4 THz.

The THz ellipticity ϵ reported in Fig. 3(a) does not vary linearly with frequency, as found, for instance, for x-cut quartz [23]. If this was the case the material would act as a quarter-wave plate ($\theta = \pi/2$) at half the frequency that it acts as a half-wave plate. The nonlinearity of ϵ with frequency is the consequence of a frequency-dependent Δn, which results from the different oscillator frequencies and strengths of the A^1_{2u} and E^1_u modes created by the rhombohedral distortion. Upon lowering the sample temperature below room temperature, enhancing the octahedral rotation [4], the frequency at which $\theta = \pi$ is lowered, as the transmission spectra in Fig. 4(a) indicate. A reduced temperature thus enhances the anisotropy, leading to a greater Δn_π, as shown in Fig. 4(b).

In summary, polarization-resolved THz-TDS was utilized to examine the distorted perovskite $LaAlO_3$, which was found to be optically anisotropic. The modification of the polarization state of THz radiation was demonstrated using [001] oriented crystals. $LaAlO_3$ may, therefore, be used to fabricate THz quarter- and half-wave plates, although a precise control of twin domain size is required to achieve the desired birefringence. Rather than a linear change in the THz ellipticity with frequency

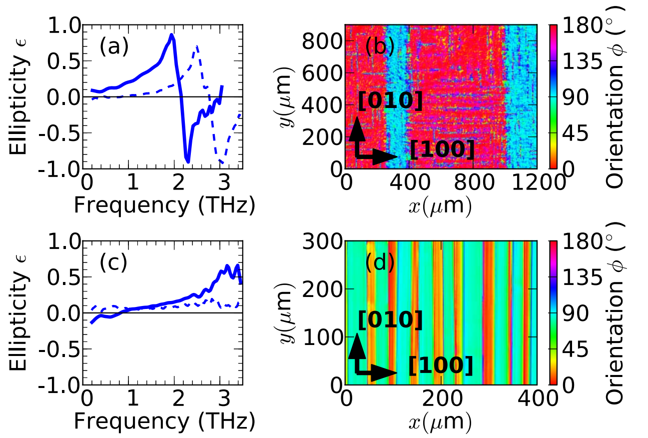

Fig. 3. THz ellipticity and optical twin domains in two [001] $LaAlO_3$ crystals. In (a) the ellipticity of the THz beam transmitted through sample A alters upon thinning from 500 μm (solid line) to 387 μm (dashed line). Polarization microscope images (520 nm) of the twin orientation show wider domains in sample A [panel (b)] than in sample B [panel (d)]. In (c) the THz ellipticity for sample B (solid line) is substantially lower, and is comparable to that of the incident THz beam (dashed line).

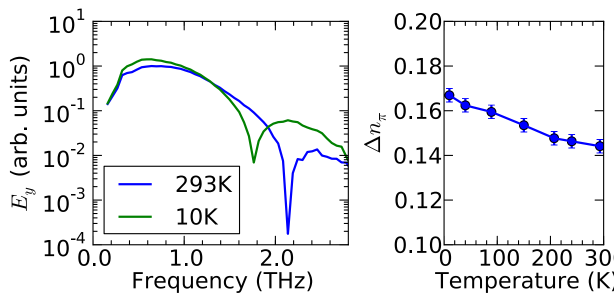

Fig. 4. (a) Spectra of THz pulse after transmission through 0.5 mm thick $LaAlO_3$ sample $[001]_A$ at room temperature and 10 K, for the incident and transmitted electric field along the y axis. (b) Temperature-dependent birefringence Δn_π calculated from the frequency at which the material acts as a half-wave plate.

(as for x-cut quartz waveplates), $LaAlO_3$ exhibits a rapid change in ellipticity as a result of a frequency-dependent birefringence.

This work was supported by the EPSRC (UK), grant EP/H003444/2. The authors would like to thank Prof. P. Thomas for the use of a polarization microscope.

References

1. J. Wang, J. B. Neaton, H. Zheng, V. Nagarajan, S. B. Ogale, B. Liu, D. Viehland, V. Vaithyanathan, D. G. Schlom, U. V. Waghmare, N. A. Spaldin, K. M. Rabe, M. Wuttig, and R. Ramesh, Science **299**, 1719 (2003).
2. A. Ohtomo and H. Y. Hwang, Nature **427**, 423 (2004).
3. N. Reyren, S. Thiel, A. D. Caviglia, L. F. Kourkoutis, G. Hammerl, C. Richter, C. W. Schneider, T. Kopp, A. S. Ruetschi, D. Jaccard, M. Gabay, D. A. Muller, J. M. Triscone, and J. Mannhart, Science **317**, 1196 (2007).
4. S. A. Hayward, F. D. Morrison, S. A. T. Redfern, E. K. H. Salje, J. F. Scott, K. S. Knight, S. Tarantino, A. M. Glazer, V. Shuvaeva, P. Daniel, M. Zhang, and M. Carpenter, Phys. Rev. B **72**, 054110 (2005).
5. K. I. Doig, F. Aguesse, A. K. Axelsson, N. M. Alford, S. Nawaz, V. R. Palkar, S. P. P. Jones, R. D. Johnson, R. A. Synowicki, and J. Lloyd-Hughes, Phys. Rev. B **88**, 094425 (2013).
6. C. Cen, S. Thiel, G. Hammerl, C. W. Schneider, K. E. Andersen, C. S. Hellberg, J. Mannhart, and J. Levy, Nat. Mater. **7**, 298 (2008).
7. M. A. Carpenter, S. V. Sinogeikin, J. D. Bass, D. L. Lakshtanov, and S. D. Jacobsen, J. Phys. Condens. Matter **22**, 035403 (2010).
8. P. Delugas, V. Fiorentini, and A. Filippetti, Phys. Rev. B **71**, 134302 (2005).
9. X. Luo and B. Wang, J. Appl. Phys. **104**, 053503 (2008).
10. P. Calvani, M. Capizzi, F. Donato, P. Dore, S. Lupi, P. Maselli, and C. P. Varsamis, Physica C **181**, 289 (1991).
11. M. V. Abrashev, A. P. Litvinchuk, M. N. Iliev, R. L. Meng, V. N. Popov, V. G. Ivanov, R. A. Chakalov, and C. Thomsen, Phys. Rev. B **59**, 4146 (1999).
12. D. Grischkowsky and S. Keiding, Appl. Phys. Lett. **57**, 1055 (1990).
13. X. Q. Zou, M. He, D. Springer, D. Lee, S. K. Nair, S. A. Cheong, T. Wu, C. Panagopoulos, D. Talbayev, and E. E. M. Chia, AIP Adv. **2**, 012120 (2012).
14. R. E. Newnham, *Properties of Materials* (Oxford University, 2005).
15. E. Castro-Camus, J. Infrared Millim. Terahz. Waves **33**, 418 (2012).
16. J. Lloyd-Hughes and T.-I. Jeon, J. Infrared Millim. Terahz. Waves **33**, 871 (2012).
17. N. C. J. van der Valk, W. A. M. van der Marel, and P. C. M. Planken, Opt. Lett. **30**, 2802 (2005).
18. T. Shimada, K. Kakimoto, and H. Ohsato, J. Eur. Ceram. Soc. **25**, 2901 (2005).
19. K. Wiesauer and C. Jördens, J. Infrared Millim. Terahz. Waves **34**, 663 (2013).
20. T. Nagashima, M. Tani, and M. Hangyo, J. Infrared Millim. Terahz. Waves **34**, 740 (2013).
21. T. Arikawa, Q. Zhang, L. Ren, A. A. Belyanin, and J. Kono, J. Infrared Millim. Terahz. Waves **34**, 724 (2013).
22. E. Castro-Camus and M. B. Johnston, J. Opt. A **11**, 105206 (2009).
23. E. Castro-Camus, J. Lloyd-Hughes, L. Fu, H. H. Tan, C. Jagadish, and M. B. Johnston, Opt. Express **15**, 7047 (2007).